


Time-optimal control of collisional $\sqrt{\text{SWAP}}$ gates in ultracold atomic systems

Jesper Hasseriis Mohr Jensen,^{*} Jens Jakob Sørensen, Klaus Mølmer, and Jacob Friis Sherson[†]
 Department of Physics and Astronomy, Aarhus University, Ny Munkegade 120, 8000 Aarhus C, Denmark

 (Received 19 July 2019; revised manuscript received 27 September 2019; published 12 November 2019)

We use quantum optimal control to identify fast collision-based two-qubit $\sqrt{\text{SWAP}}$ gates in ultracold atoms. We show that a significant speedup can be achieved by optimizing the full gate instead of separately optimizing the merge-wait-separate sequence of the trapping potentials. Our optimal strategy does not rely on the atoms populating the lowest eigenstates of the merged potential, and it crucially includes the accumulation of quantum phases before the potentials are fully merged. Our analyses transcend the particular trapping geometry, but for comparison with previous works, we present systematic results for an optical lattice and find greatly improved gate durations and fidelities.

DOI: [10.1103/PhysRevA.100.052314](https://doi.org/10.1103/PhysRevA.100.052314)

I. INTRODUCTION

Optically trapped ultracold atomic systems have enjoyed impressive recent progress with regard to their preparation and the control of both internal and external degrees of freedom [1–4]. Especially, recent advances [5–16] have augmented the viability of using the long coherence times of their spin internal degrees of freedoms for quantum computing [17–26]. While single-qubit operations with fidelities above 0.99 have been demonstrated in multiple experiments [27,28], corresponding fidelities of two-qubit entangling operations are still the subject of research [29–37]. Entangling two-qubit gates can be mediated by long-range interactions such as dipole-dipole interactions between Rydberg atoms [19,38–40]. Although the long-range nature of these interactions allows potentially fast operations, their use of highly excited atomic states make them vulnerable to enhanced coupling to the environment.

Short-range collisional (contact) interactions provide an alternative for neutral atom quantum gates [30,35,41–47]. Merging two initially separated atoms into a common trap initiates a collisional interaction depending on the exchange symmetry of the atomic wave function and hence of the spin state of the atoms. After a duration determined by the interaction strength in the merged state, the atoms are spatially separated, and under appropriate conditions, the simple three-stage merge-wait-separate sequence illustrated in Fig. 1 realizes the entangling $\sqrt{\text{SWAP}}$ gate.

The short-range character of the collisions ensures that only the desired qubits participate in the operation, decreasing the detrimental coupling to other qubits and to the environment. Relying on collisional interaction imposes strong requirements for the precision with which the spatial degree of freedom of the atoms must be controlled. Current experimental control protocols performing this entangling gate achieve

this by remaining adiabatic with respect to the external potential, but this severely limits the total number of gate operations before decoherence effects become significant [30,35].

Finding fully diabatic, high-quality control protocols is a task well suited for quantum optimal control. Previous works [48,49] have thus reduced the duration of the merging stage in optical geometries by orders of magnitude compared to adiabatic solutions. However, the current best results for the merging stage have thus far not crossed the 0.99 threshold. This is especially detrimental since even slight merging errors also reduce the quality of subsequent waiting and separation stages. To our knowledge, no optimization of the full gate has been carried out.

In this paper, we discuss how the $\sqrt{\text{SWAP}}$ gate relies on the evolution of a relative phase between singlet and triplet spin-state components and why the partial accumulation of this phase already during the merging stage is a challenge for the optimization of stagewise protocols. We develop means to solve this challenge, and we proceed to show that a protocol without dedicated merge-wait-separate stages yields a faster performance and 0.99 fidelity for the full $\sqrt{\text{SWAP}}$ operation with ultracold ^{87}Rb atoms. We stress that our considerations of the accumulated relative phase and the full gate optimization

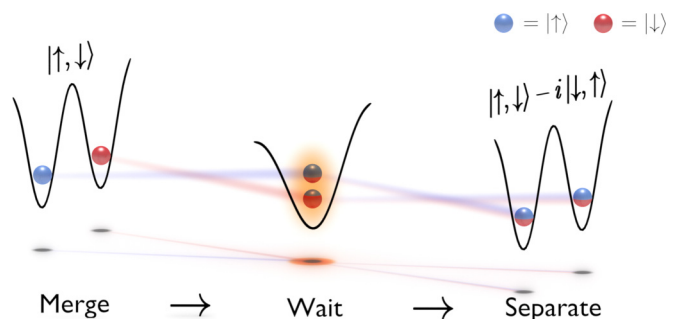


FIG. 1. Schematic of the merge-wait-separate sequence implementing the $\sqrt{\text{SWAP}}$ gate. Completing the sequence transfers a state of initially opposite spins into a spin-entangled state.

^{*}jhasseriis@phys.au.dk

[†]sherson@phys.au.dk

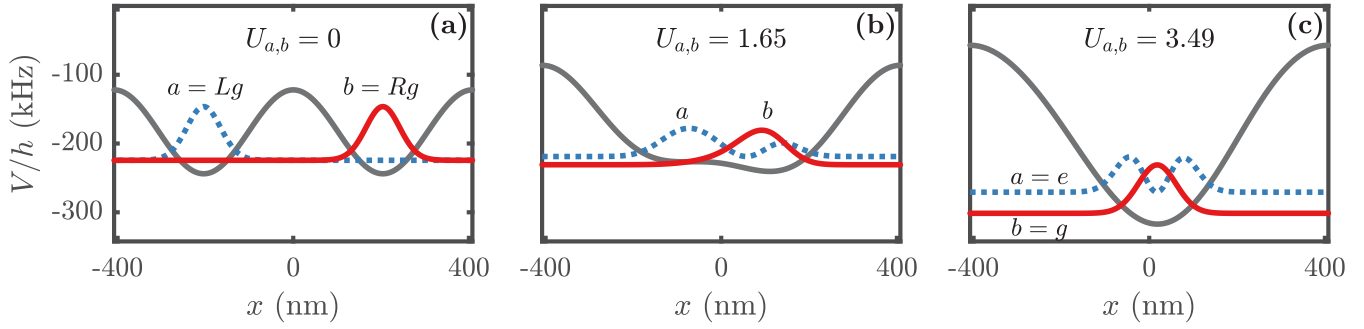


FIG. 2. Merging stage ($\beta = 0.52\pi \times t/T$, $\theta = -0.474\pi$, $V_0/h = 122$) kHz of the lattice unit cell in the independent-particle picture. (a) $t = 0$: Atoms are initially prepared in the separated double-well configuration. (b) $t = 0.7T$: Intermediate snapshot of the merging process. (c) $t = T$: Atoms occupy orthogonal states in the merged single-well configuration. In each snapshot the value of the energy difference $U_{a,b}$ between corresponding $|\Psi_{a,b}^\pm\rangle$ is shown in units of $\text{kHz} \cdot h$ [see Eqs. (6)–(9)].

are independent of the specific physical problem geometry, atomic species, model dimensionality, and collisional gate type.

The paper is organized as follows. In Sec. II we present the trapping geometry under consideration for the $\sqrt{\text{SWAP}}$ operation. In Sec. III we present the theory for implementing the $\sqrt{\text{SWAP}}$ gate in ultracold atoms. The two-particle Hamiltonian is introduced and general properties of the allowed states are discussed. Initially, we use symmetrized product states to construct the computational basis states. Using these states, we describe the important accumulated relative phase during the merging sequence. Central features of the phase accumulation are illustrated in an independent-particle picture in which the spatial distribution remains unaffected by the interaction. In our numerical optimization, we do not rely on independent particles but propagate genuine two-particle wave functions for the interacting atoms. In Sec. IV we discuss the difference between the staged merge-wait-separate approach and the full gate approach in terms of optimal trajectories in Hilbert space. In Sec. V we present and discuss the results. In Sec. VI we provide a brief outlook for possible future work and in Sec. VII we summarize the main conclusions of the paper.

II. TRAPPING GEOMETRY

A necessary feature of any candidate geometry for the collisional $\sqrt{\text{SWAP}}$ operation is the possibility of bringing two atoms from a separated configuration into contact by, for example, merging them in a common trap as illustrated in Fig. 1. We consider the implementation with an optical lattice [30,50] that has been loaded with a Mott state of unit filling and where the atoms at every other site have been prepared with opposite spin states. An analysis presented in Appendix A justifies a one-dimensional (1D) description with the potential

$$V(x) = -V_0 \left[\cos^2\left(\frac{\beta}{2}\right) \left\{ 1 + \cos^2\left(kx - \frac{\pi}{2}\right) \right\} + \sin^2\left(\frac{\beta}{2}\right) \left\{ 1 + \cos\left(kx - \theta - \frac{\pi}{2}\right) \right\}^2 \right]. \quad (1)$$

Here V_0 provides the overall lattice depth, while β and θ adjust the height and tilt of adjacent wells. By controlling

$\{\beta(t), \theta(t), V_0(t)\}$, pairs of adjacent wells are transformed from a double-well into a single-well configuration as illustrated in Fig. 2. In an independent-particle picture, the atom in the ground state of the Left (Right) well is transferred to the first excited (ground) state of the merged well, $|Lg\rangle|Rg\rangle \rightarrow |e\rangle|g\rangle$.

III. $\sqrt{\text{SWAP}}$ GATE WITH COLD ATOMS

The $\sqrt{\text{SWAP}}$ gate is concerned with the qubit, i.e., spin degrees of freedom of the atoms, and its simplest implementation is through the three-stage merge-wait-separate sequence in Fig. 1. In this section, we recall the theory behind this procedure.

The system is described by the effective Hamiltonian

$$\hat{H} = \sum_{i=1}^2 \hat{h}(x_i) + g_{1D} \delta(x_1 - x_2). \quad (2)$$

Here, x_i are the coordinates of the two atoms, and $\hat{h}(x) = -\frac{\hbar^2}{2m} \frac{\partial^2}{\partial x^2} + V(x)$ is the single-particle Hamiltonian with trapping potential V . The form of the interaction term and the value of the coupling strength g_{1D} are discussed in Appendix A.

We use identical bosonic atoms and the full two-particle state can thus be expanded on symmetric states of the form

$$|\Phi^{\uparrow\uparrow}\rangle = |\Psi^+\rangle|\chi^{\uparrow\uparrow}\rangle, \quad |\Phi^{\downarrow\downarrow}\rangle = |\Psi^+\rangle|\chi^{\downarrow\downarrow}\rangle, \quad (3)$$

$$|\Phi^\pm\rangle = |\Psi^\pm\rangle|\chi^\pm\rangle, \quad (4)$$

with the symmetric (+) spin triplet and antisymmetric (−) spin singlet states

$$|\chi^\pm\rangle = |\uparrow\rangle_1|\downarrow\rangle_2 \pm |\downarrow\rangle_1|\uparrow\rangle_2 \quad (5)$$

and symmetric (+) and antisymmetric (−) spatial states $|\Psi^\pm\rangle$, where proper normalization is implied in the remainder of the paper.

The Hamiltonian (2) is independent of the spin degrees of freedom and cannot induce transitions between states of different total spin. The interaction term $g_{1D}\delta(x_1 - x_2)$ only acts on the Ψ^+ component since $\Psi^-(x_1, x_2 = x_1) = 0$ by construction. This introduces an energy difference between

the otherwise degenerate singlet and the triplet state vector components. This energy difference is the main mechanism behind the $\sqrt{\text{SWAP}}$ gate.

A. Symmetrized product states

To illustrate the dynamics leading to the $\sqrt{\text{SWAP}}$ operation we consider an approximate analysis with symmetrized product states, but we emphasize that our numerical optimization is carried out with the full two-particle interaction dynamics.

We associate the qubits with the spins of atoms occupying definite spatial states. If $|a\rangle$ and $|b\rangle$ denote such single-particle eigenstates of $\hat{h}(x)$, spatially symmetrized product states

$$|\Psi_{a,b}^{\pm}\rangle = |a\rangle_1|b\rangle_2 \pm |b\rangle_1|a\rangle_2 \quad (6)$$

are approximate (as discussed in Sec. III B) eigenstates of \hat{H} with energies

$$\langle\Psi_{a,b}^{-}|\hat{H}|\Psi_{a,b}^{-}\rangle = E_a + E_b, \quad (7)$$

$$\langle\Psi_{a,b}^{+}|\hat{H}|\Psi_{a,b}^{+}\rangle = E_a + E_b + U_{a,b}, \quad (8)$$

where E_a and E_b are single-particle energies and

$$U_{a,b} \equiv 2 \int_{-\infty}^{\infty} |a(x)|^2 |b(x)|^2 g_{1D}(x) dx. \quad (9)$$

The energy difference between $|\Psi_{a,b}^{\pm}\rangle$ clearly depends on the spatial overlap of the two atoms and the collisional coupling strength.

Using (6) in (3) and (4), we define symmetrized computational basis states for the $\sqrt{\text{SWAP}}$ operation:

$$|\uparrow_a, \downarrow_b\rangle \equiv |\uparrow_a\rangle_1|\downarrow_b\rangle_2 + |\downarrow_b\rangle_1|\uparrow_a\rangle_2 = |\Phi_{a,b}^{+}\rangle + |\Phi_{a,b}^{-}\rangle, \quad (10)$$

$$|\downarrow_a, \uparrow_b\rangle \equiv |\downarrow_a\rangle_1|\uparrow_b\rangle_2 + |\uparrow_b\rangle_1|\downarrow_a\rangle_2 = |\Phi_{a,b}^{+}\rangle - |\Phi_{a,b}^{-}\rangle, \quad (11)$$

$$|\uparrow_a, \uparrow_b\rangle \equiv |\uparrow_a\rangle_1|\uparrow_b\rangle_2 + |\uparrow_b\rangle_1|\uparrow_a\rangle_2 = |\Phi_{a,b}^{\uparrow\uparrow}\rangle, \quad (12)$$

$$|\downarrow_a, \downarrow_b\rangle \equiv |\downarrow_a\rangle_1|\downarrow_b\rangle_2 + |\downarrow_b\rangle_1|\downarrow_a\rangle_2 = |\Phi_{a,b}^{\downarrow\downarrow}\rangle. \quad (13)$$

We see in the first two equations that the relative phase between the triplet and the singlet components is essential to determine how the spins are correlated with the spatial states of the atoms. The last two equations represent states that are unaffected by the $\sqrt{\text{SWAP}}$ operation and acquire only the same phase factor as the (+) components in the first two equations.

We define the $\sqrt{\text{SWAP}}$ gate in states (10)–(13) as

$$|\uparrow_a, \downarrow_b\rangle \rightarrow \sqrt{\text{SWAP}}|\uparrow_a, \downarrow_b\rangle = |\uparrow_a, \downarrow_b\rangle - i|\downarrow_a, \uparrow_b\rangle, \quad (14)$$

$$|\downarrow_a, \uparrow_b\rangle \rightarrow \sqrt{\text{SWAP}}|\downarrow_a, \uparrow_b\rangle = -|\uparrow_a, \downarrow_b\rangle - i|\downarrow_a, \uparrow_b\rangle, \quad (15)$$

$$|\uparrow_a, \uparrow_b\rangle \rightarrow \sqrt{\text{SWAP}}|\uparrow_a, \uparrow_b\rangle = e^{-i\pi/4}|\uparrow_a, \uparrow_b\rangle, \quad (16)$$

$$|\downarrow_a, \downarrow_b\rangle \rightarrow \sqrt{\text{SWAP}}|\downarrow_a, \downarrow_b\rangle = e^{-i\pi/4}|\downarrow_a, \downarrow_b\rangle. \quad (17)$$

If the spins are initially in opposite states, the $\sqrt{\text{SWAP}}$ operation yields an entangled state. If the spins are initially equal a phase $e^{-i\pi/4}$ is applied. In the following, we focus on the mapping (14) and study the approximate system dynamics to

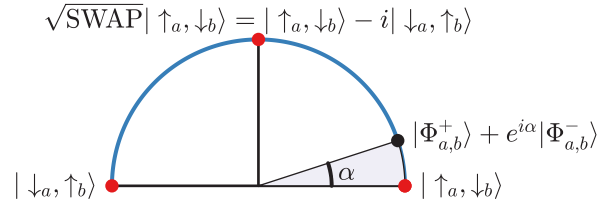


FIG. 3. Illustration of how the spins are distributed due to the relative phase in the first two quadrants. Here $\alpha = \pi/10$.

find the necessary conditions for implementing the $\sqrt{\text{SWAP}}$ gate.

1. Time evolution in a static trap

If $|a\rangle$ and $|b\rangle$ are single-particle eigenstates of $\hat{h}(x)$, the time evolution of $|\uparrow_a, \downarrow_b\rangle = |\Phi_{a,b}^{+}\rangle + |\Phi_{a,b}^{-}\rangle$ is approximately given by

$$|\Phi_{a,b}(t)\rangle \approx |\Phi_{a,b}^{+}\rangle + e^{i\alpha}|\Phi_{a,b}^{-}\rangle \quad (18)$$

$$\rightarrow \cos\left(\frac{\alpha}{2}\right)|\uparrow_a, \downarrow_b\rangle - i\sin\left(\frac{\alpha}{2}\right)|\downarrow_a, \uparrow_b\rangle, \quad (19)$$

where we disregard global phases as the dynamics of the system and the spin distribution on the atoms is fully described by the relative phase $\alpha(t) = U_{a,b}t/\hbar$ between the state components. After the duration $T_{\text{SWAP}} = \pi\hbar/U_{a,b}$ ($\alpha = \pi$) the spins are fully swapped $|\downarrow_a, \uparrow_b\rangle$, while the interaction for half of this duration $T_{\sqrt{\text{SWAP}}} = T_{\text{SWAP}}/2$ ($\alpha = \pi/2$) implements the desired $\sqrt{\text{SWAP}}$ gate as illustrated in Fig. 3.

The spin swapping rate $\dot{\alpha} \propto U_{a,b}$ depends only on the interaction energy, Eq. (9), which remains constant throughout the evolution in a static trap. To obtain a finite $T_{\sqrt{\text{SWAP}}}$ the atoms must therefore be sufficiently overlapping. This condition is satisfied in the merged configuration but clearly not in the initial configuration [see Figs. 2(a) and 2(c)].

2. Time evolution in an adiabatically transformed trap

Suppose the trapping potential is transformed adiabatically with respect to the single-particle states such that $a = a(t)$ and $b = b(t)$ follow instantaneous eigenstates of $\hat{h}(x)$. Then the time evolution given by Eq. (19) remains valid with $\alpha(t) = \hbar^{-1} \int_0^t U_{a(t'),b(t')} dt'$. The spin swapping rate $\dot{\alpha} \propto U_{a(t),b(t)}$ is now time dependent and becomes nonzero as the atoms begin to overlap.

As a consequence, the phase accumulated during the merging is in general $\alpha(T) \neq 0$, which reduces the waiting stage duration needed to obtain the entangled state. This is clearly shown in Fig. 3 if we let $\alpha = \alpha(T)$; the phase acquired during merging already brings the state closer to $\sqrt{\text{SWAP}}|\uparrow_a, \downarrow_b\rangle$. An additional $\alpha(T)$ will be acquired during the separation stage. Assuming, for simplicity, $\alpha(T) \leq \pi/4$, the $\sqrt{\text{SWAP}}$ duration is reduced to $T_{\sqrt{\text{SWAP}}} = (\pi/2 - 2\alpha(T))\hbar/U_{a(T),b(T)}$, where the factor 2 accounts for both the merging and the separation stage. Labeling explicitly the merging duration by $T \rightarrow T^m$, the total duration of the full gate operation using the merge-separate sequence is then $T^f = 2T^m + T_{\sqrt{\text{SWAP}}}$.

This sequence explicitly implements the mapping of a single basis state, (14). Fortunately, this sequence also

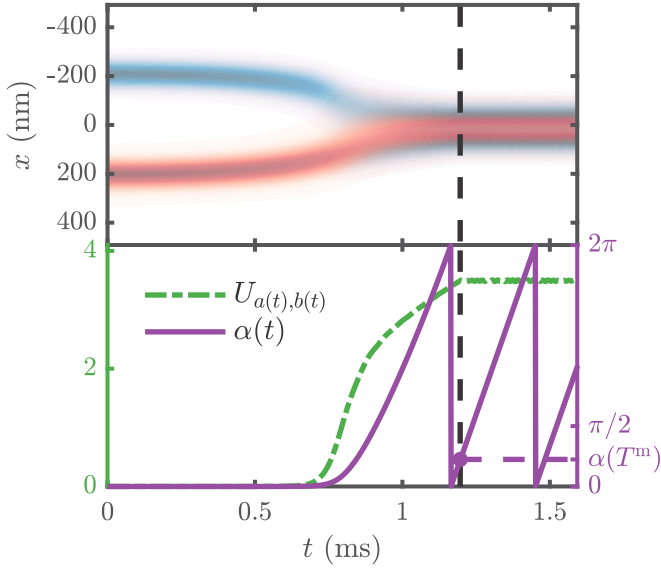


FIG. 4. Adiabatic lattice merging of the atoms into a single-well configuration as in Fig. 2. Top: Density plots $|a(x, t)|^2$ (top, blue shade) and $|b(x, t)|^2$ (bottom, red shade) of single-particle states $|a(0)\rangle|b(0)\rangle = |Lg\rangle|Rg\rangle \rightarrow |e\rangle|g\rangle$ [51]. The merge duration T^m is marked by the dashed line and at $t > T^m$ the potential is static. Bottom: Interaction energy $U_{a(t), b(t)}$, Eq. (9) (dash-dotted green line), and total accumulated relative phase $\alpha(t) = \hbar^{-1} \int_0^t U_{a(t'), b(t')} dt'$ (solid purple line). The phase acquired during merging $\alpha(T^m)$ is nonzero.

simultaneously realizes the remaining mappings. The mapping (15) simply corresponds to starting at $\alpha(0) = \pi$, from which the phase accumulation proceeds identically to above. For the mappings (16) and (17), note that (14) implies correct, simultaneous preparation of the individual triplet and singlet components since there is no coupling between states of different symmetry. Thus, these mappings are also guaranteed to be realized. We note at this point that the converse is not necessarily true: a sequence implementing mappings (16) and (17) does not guarantee the mappings (14) and (15) since the singlet component is absent.

To summarize the ideas developed in this section, we show a numerical example of the accumulated phase to illustrate qualitative features in Fig. 4. Here, the system from Fig. 2 is adiabatically merged and followed by a holding time in the static final potential [51]. In this independent-particle picture, the single-particle states are propagated independently, with the interaction affecting only the relative phase and not the spatial distribution, which is the approximation made in Eq. (18). At each point in time we construct $|\Psi_{a(t), b(t)}^\pm\rangle$ and calculate the corresponding $U_{a(t), b(t)}$. As the atoms begin to overlap the relative phase accumulates, resulting in $\alpha(T^m) \approx \pi/4$. Following the merge, the $\sqrt{\text{SWAP}} |\uparrow_e, \downarrow_g\rangle$ state is obtained after the short, static holding time of about 0.04 ms. If instead the atoms were immediately separated, the $\sqrt{\text{SWAP}} |\uparrow_{Lg}, \downarrow_{Rg}\rangle$ state would be obtained since $2\alpha(T^m) \approx \pi/2$.

The adiabatic transfer thus ensures a high-fidelity implementation of the $\sqrt{\text{SWAP}}$ gate since we are guaranteed to stay within the superposition of just one singlet and triplet state Eq. (18). However, for the purposes of quantum computation we also need the implementation to be fast. The speedup is

achieved by exploiting the interference effects of many intermediately populated excited states. To enable the engineering of these very complicated fully diabatic transfers we turn to quantum optimal control. Before doing so, we close this section by replacing the symmetrized product states with the true two-particle eigenstates.

B. Two-particle eigenstates

The analysis of the dynamics in the previous section approximated the symmetrized product states $|\Psi_{a,b}^\pm\rangle$ Eq. (6) to be eigenstates of $\hat{H}(x_1, x_2)$, where $|a\rangle$ and $|b\rangle$ were eigenstates of $\hat{h}(x)$. In the limit of vanishing interactions (no spatial overlap or zero coupling) this approximation is exact. This allows us to relate to the true spatial two-particle eigenstates (annotated by \sim) in the following way:

$$|\tilde{\Psi}_{a,b}^-\rangle = |\Psi_{a,b}^-\rangle, \quad (20)$$

$$|\tilde{\Psi}_{a,b}^+\rangle \rightarrow |\Psi_{a,b}^+\rangle, \quad (21)$$

where \rightarrow in this context implies vanishing interactions. Due to symmetrization properties, only the triplet state is affected by the interaction ($|\tilde{\Psi}_{a,b}^+\rangle$ has less diagonal population $x_1 = x_2$ relative to $|\Psi_{a,b}^+\rangle$). This notation is very convenient since we retain reference to the intuitive independent-particle picture. In particular, the analysis following Eq. (6) is still valid upon annotating all states and energies with \sim . The approximation made in Eq. (18) consisted in ignoring the small interaction matrix elements between different triplet states (other off-diagonal elements vanish identically) such that the symmetrized product states $|\Psi_{a,b}^\pm\rangle$ were approximate eigenstates of the full Hamiltonian. Using the true eigenstates $|\tilde{\Psi}_{a,b}^\pm\rangle$, the results are exact.

It is also possible to describe the dynamics in a static potential with an effective spin Hamiltonian $\hat{H}_{\text{spin}} = J_{\text{ex}} \cdot \hat{\mathbf{S}}_1 \otimes \hat{\mathbf{S}}_2$ even though the spin swapping is purely due to spatial effects (extension to the adiabatic case is straightforward). This is also known as the exchange interaction. Here $\hat{\mathbf{S}}_i$ are spin operators and $J_{\text{ex}} = U_{a,b}$ is the exchange energy. See Appendix C for a brief derivation of this result.

IV. QUANTUM OPTIMAL CONTROL OF $\sqrt{\text{SWAP}}$ IN ULTRACOLD ATOMS

In Sec. III we showed that the desired $\sqrt{\text{SWAP}}$ operation can be implemented based on a single basis state mapping, $|\uparrow_{Lg}, \downarrow_{Rg}\rangle \rightarrow \sqrt{\text{SWAP}} |\uparrow_{Lg}, \downarrow_{Rg}\rangle$. Formulating this as a state transfer control problem, the initial and target states for the full gate are

$$|\Phi_0\rangle = |\tilde{\Phi}_{Lg,Rg}^+\rangle + |\tilde{\Phi}_{Lg,Rg}^-\rangle, \quad (22)$$

$$|\Phi_t^f\rangle = |\tilde{\Phi}_{Lg,Rg}^+\rangle + e^{i\pi/2} |\tilde{\Phi}_{Lg,Rg}^-\rangle. \quad (23)$$

By writing the states in terms of singlet and triplet components we emphasize the goal of ultimately establishing the correct relative phase in the separated configuration by letting the atoms collide. See Appendix B for a description of methods and problem parameters.

A simplified approach to solving the control problem $|\Phi_0\rangle \rightarrow |\Phi_t^f\rangle$ is to use the merge-wait-separate sequence. The

problem can then be reduced to optimizing just the merging stage, as the associated optimal controls can be extended to implement the whole sequence: the waiting stage duration is determined by the relative phase $\alpha(T^m)$ acquired during the optimized merging stage, whereas the separation stage is carried out by propagating along the time-inverted optimized merging control. A suitable target state for the merging subproblem is

$$|\Phi_t^m\rangle = |\tilde{\Phi}_{e,g}^+\rangle + e^{i\alpha} |\tilde{\Phi}_{e,g}^-\rangle. \quad (24)$$

The merging subproblem thus consists in realizing $|\Phi_0\rangle \rightarrow |\Phi_t^m\rangle$. This target state is not stationary and will exhibit two-level beating dynamics if the transfer is successful. Note the inclusion of a target relative phase $\alpha_t \leq \pi/4$. This is because $\alpha(t)$ is monotonically increasing due to $\tilde{U} \geq 0$. If the target phase is excluded ($\alpha_t = 0$), then in an independent-particle picture, the optimizer will try to minimize the time-integrated overlap between the atomic states during the transfer. This is contradictory to the overall goal of the merging, which is exactly to overlap the atoms to enable the spin swapping. The total accumulated phase is not crucial to the overall $\sqrt{\text{SWAP}}$ operation since one may simply adjust the duration of the waiting stage. It follows that any final superposition of $|\tilde{\Phi}_{e,g}^\pm\rangle$ is acceptable as long as $\alpha(T) \leq \pi/4$. In fact, a nonzero phase within this range is beneficial, as it speeds up the overall gate operation (see Fig. 3). However, the standard figure of merit for the state transfer quality is the fidelity

$$\mathcal{F} = |\langle \Phi_t | \Phi(T) \rangle|^2, \quad (25)$$

which for the merging subproblem, $|\Phi_t\rangle = |\Phi_t^m\rangle$, depends on the chosen target phase. In this case a more appropriate measure of the transfer quality insensitive to the relative phase is the total population in $|\tilde{\Phi}_{e,g}^\pm\rangle$,

$$\mathcal{F}' = |\langle \tilde{\Phi}_{e,g}^+ | \Phi(T) \rangle|^2 + |\langle \tilde{\Phi}_{e,g}^- | \Phi(T) \rangle|^2 \geq \mathcal{F}, \quad (26)$$

where $\mathcal{F} = \mathcal{F}'$ only when $\alpha(T) = \alpha_t$. Thus, optimizing \mathcal{F}' would alleviate the constraint on the relative phase. Instead of doing this, we simply use \mathcal{F}' as a stopping condition and optimize \mathcal{F} with an appropriate target phase such that $\mathcal{F} \approx \mathcal{F}'$. For the durations $T = T^m$ under consideration, numerical investigations suggest typical values of $\alpha(T^m) \in [0.31, 0.44] \approx [\pi/10, \pi/7]$. This is well below $\pi/4$. We find a suitable target phase to be $\alpha_t = 0.33$. The optimization could be improved by making an appropriate cost functional replacement $J_{\mathcal{F}} \rightarrow J_{\mathcal{F}'}$ and deriving the resulting optimality system.

Previous works [48,49] considered only the merging subproblem and did not include the singlet component in the initial or the target state, using only the triplet component. This corresponds to realizing the mappings (16) and (17), which as previously mentioned does not guarantee simultaneous implementation of the remaining mappings, (14) and (15), but may still be considered an approximation. Additionally, ignoring the singlet component reduces the problem difficulty since the optimization no longer has to achieve a relative phase.

The merit of solving the full control problem by reducing it to the merging subproblem is its conceptual simplicity. From a numerical point of view, it also typically involves a reduced interval of time integration. This is substantial due to the low

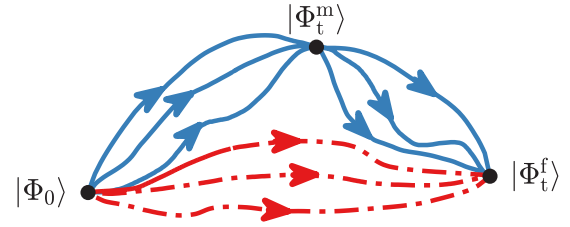


FIG. 5. Schematic of different idealized optimal trajectories in Hilbert space, both leading to $\sqrt{\text{SWAP}} (|\uparrow_{Lg}, \downarrow_{Rg}\rangle)$. The three upper trajectories (solid blue curves) corresponds to implementing the simple merge-wait-separate sequence. In this case, each trajectory must pass through $|\Phi_t^m\rangle$, whence it can be connected to $|\Phi_t^f\rangle$ as explained in the text. The three lower trajectories (dash-dotted red curves) correspond to implementing the full gate without distinct stages. Here there is no requirement to pass through a particular intermediate state.

time resolution required to faithfully simulate the interaction δ function. Nevertheless, there are several drawbacks to this approach. First, optimizing towards $|\Phi_t^m\rangle$ is an artificial and unnecessarily strict condition. It can be understood as forcing the optimal state trajectories to pass through a particular intermediate point (or small volume in the case of \mathcal{F}') in Hilbert space as illustrated by the upper trajectories in Fig. 5. Second, extending optimal controls to implement the complete merge-wait-separate sequence is predicated on idealized unit fidelity transfers with regard to $|\Phi_t^m\rangle$. Even 0.99 fidelity solutions will have their errors exacerbated throughout the waiting and separation stages, causing alterations to the state trajectory away from $|\Phi_t^f\rangle$, which is the state we are ultimately interested in obtaining. The lower trajectories in Fig. 5 correspond to optimizing the full problem $|\Phi_0\rangle \rightarrow |\Phi_t^f\rangle$ directly and are not required to pass through any particular intermediate state. The control problem is not broken up into distinct stages and becomes much less restrictive. We note that this conclusion not only pertains to the present $\sqrt{\text{SWAP}}$ problem, but extends to any gate implemented with a stagewise protocol (see, e.g., Refs. [43,44,46,52]).

In this work we combine the two approaches. We first optimize towards $|\Phi_t^m\rangle$ in the merging subproblem. We subsequently extend the corresponding optimized controls to implement the full gate. These extended controls are then used as seeds for the optimization towards $|\Phi_t^f\rangle$ in the full gate problem. This methodology allows a fair comparison of the two approaches.

V. RESULTS

In this section we present optimization results. A solution is considered optimal if it exceeds $\mathcal{F}^m = 0.99$ in the submerging problem or $\mathcal{F}^f = 0.99$ in the full problem.

Figure 6 shows optimization results for the merging subproblem. A total of 2544 seeds were optimized, with between 100 and 250 seeds per duration. Red circles show $1 - \mathcal{F}^m$ for the best controls obtained for each T^m . We find the upper bound for the quantum speed limit to be $T_{\text{QSL}}^m \leq 0.0888$ ms (see Appendix B 2 for the corresponding time-optimal control). Compared to previous results of 0.97 fidelity [48,49]

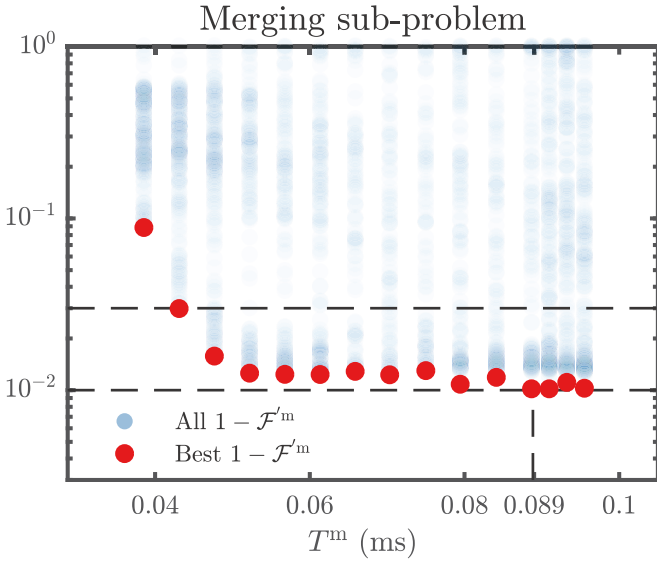


FIG. 6. Optimization results (lower is better) for the merging subproblem. The lower (upper) dashed horizontal line marks the 0.99 (0.97) fidelity threshold. $1 - \mathcal{F}^m$ is shown for each solution in a batch optimized for $\alpha_t = 0.33$. The distribution density is indicated by the translucency. The best solutions for each T are shown by filled red circles. Of 2544 seeds, only 3 optimized to $\mathcal{F}^m = 0.99$. The quantum speed limit bound in this optimization batch is $T_{\text{QSL}}^m \leq 0.0888$ ms.

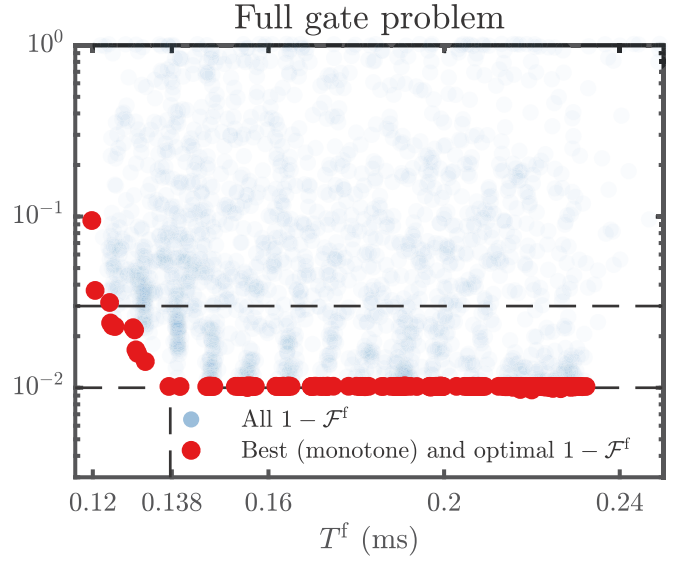


FIG. 8. Optimization results (lower is better) for the full gate problem when using the optimized extended solutions from Fig. 6 as seeds. The lower (upper) horizontal dashed line marks the 0.99 (0.97) fidelity threshold. $1 - \mathcal{F}^f$ is shown for each solution. The monotonically best and optimal solutions are shown by filled red circles. Of 2323 seeds, a total of 277 optimized to $\mathcal{F}^f = 0.99$. The quantum speed limit bound in this optimization batch is $T_{\text{QSL}}^f \leq 0.1377$ ms.

(which also use more approximations), this is still a factor of ~ 1.69 reduction in duration. Using instead 0.97 as the fidelity threshold the reduction is ~ 3.47 . Blue circles show $1 - \mathcal{F}^m$ for all optimized controls, where the translucency indicates the density distribution. From the translucency we

see that the average quality of the optimized controls increases with the duration as the problem becomes easier (the apparent increase in low-fidelity solutions for the last three durations is due to an increased overall number of seeds). Nevertheless, the best obtained fidelities plateau around 0.988 over a rather

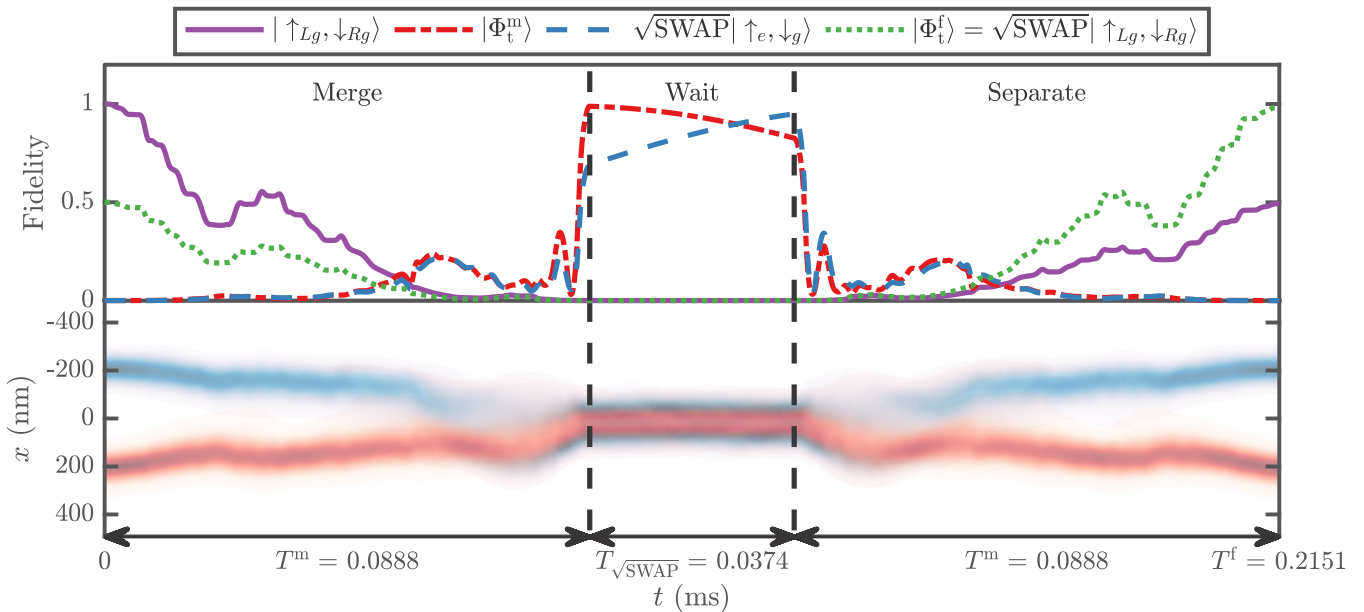


FIG. 7. Full $\sqrt{\text{SWAP}}$ gate operation based on the time-optimal merging control. The merge-wait-separate stages are indicated by the dashed vertical lines. Top: Instantaneous fidelities with various states. Bottom: Corresponding independent single-particle densities [51]. The target state $|\Phi_t^m\rangle$ is obtained at T^m with $\mathcal{F}^m = 0.99$. The system then exhibits two-level dynamics before the separation onset and enters $|\Phi_t^f\rangle$ with suboptimal final fidelity $\mathcal{F}^f = 0.983$ at T^f .

TABLE I. Figures of merit when propagating different states along the same optimized controls corresponding either to the time-optimal merging control (top row) or to the time-optimal full gate control (bottom row).

	Single particle				Two particle						T^m	T^f
	$\mathcal{F}_{Lg \rightarrow e}^m$	$\mathcal{F}_{Rg \rightarrow g}^m$	$\mathcal{F}_{Lg \rightarrow Lg}^f$	$\mathcal{F}_{Rg \rightarrow Rg}^f$	\mathcal{F}_-^m	\mathcal{F}_+^m	$\mathcal{F}_{\alpha_i=0}^m$	\mathcal{F}^m	\mathcal{F}^m	\mathcal{F}^f		
Merging optimized	0.994	0.997	0.992	0.992	0.992	0.988	0.950	0.9886	0.990	0.983	0.0888 ms	0.215 ms
Full gate optimized	0.540	0.868	0.997	0.996	0.570	0.473	0.498	0.519	0.522	0.990	0.0478 ms	0.1377 ms

long interval. As discussed previously, the full $\sqrt{\text{SWAP}}$ gate can be realized by extending the merging optimized controls. This is shown for the time-optimal controls at T_{QSL}^m in Fig. 7, where instantaneous fidelities with various states are plotted as a function of time. We also plot the corresponding independently propagated single-particle wave functions [51]. The initial state $|\uparrow_{Lg}, \downarrow_{Rg}\rangle$ is transferred into the merged trap in time $T^m = 0.0888$ ms with $\mathcal{F}^m = 0.99$ and acquires a phase of $\alpha(T^m) \approx 0.40$ during merging. The waiting stage with two-level dynamics lasts for $T_{\sqrt{\text{SWAP}}} \approx 0.0375$ ms and nearly enters the entangled $\sqrt{\text{SWAP}} |\uparrow_e, \downarrow_g\rangle$ state. The controlled termination of the exchange interaction ensures that the remaining phase is acquired in the separation stage such that the final state is approximately $\sqrt{\text{SWAP}} |\uparrow_{Lg}, \downarrow_{Rg}\rangle$ with fidelity $\mathcal{F}^f = 0.983$. The total gate time is $T^f = 2T^m + T_{\sqrt{\text{SWAP}}} = 0.215$ ms. We note that the process is fundamentally limited by the rate at which entanglement can be generated. To provide a sense of scale, $|\uparrow_e, \downarrow_g\rangle$ prepared in the merged configuration would achieve $\alpha = 0 \rightarrow \pi/2$ in $T_{\sqrt{\text{SWAP}}} = 0.078$ ms, which illustrates that there is still room for improvement.

The top row of data in Table I summarizes several figures of merit for various states when propagated along the time-optimal control. The superscripts m and f indicate whether the quantity is measured at the merging or full gate duration, respectively. Here, $\mathcal{F}_{Lg \rightarrow e}^m$ and $\mathcal{F}_{Rg \rightarrow g}^m$ are the single-particle fidelities corresponding to the merging transfer $|Lg\rangle|Rg\rangle \rightarrow |e\rangle|g\rangle$, $\mathcal{F}_{Lg \rightarrow Lg}^f$ and $\mathcal{F}_{Rg \rightarrow Rg}^f$ are the single-particle fidelities corresponding to the transfer $|Lg\rangle|Rg\rangle \rightarrow |Lg\rangle|Rg\rangle$ when extending the merging optimized control to the full gate, \mathcal{F}_\pm^m are the merging fidelities when including only the triplet (+) or singlet (-) component in the initial and target state, and $\mathcal{F}_{\alpha_i=0}^m$ is the merging fidelity if the target phase is excluded.

The high single-particle fidelities $\mathcal{F}_{Lg \rightarrow e}^m$ and $\mathcal{F}_{Rg \rightarrow g}^m$ indicate that the imperfection in \mathcal{F}^m is mainly due to the interaction affecting the triplet and singlet components differently. A supporting observation is that $\mathcal{F}_-^m \gtrsim 0.99$ while $\mathcal{F}_+^m \lesssim 0.99$. This shows that the relative phase acquired during the merging is a small but significant effect for producing high-quality solutions. Additionally, upon comparing $\mathcal{F}_{\alpha_i=0}^m$ and \mathcal{F}^m we explicitly see that fidelity is not the best figure of merit for the merging subproblem, but using \mathcal{F}^m as a stopping condition for the optimization is still a viable solution.

In Fig. 8 we show optimization results for the full gate problem, using optimized merging controls as seeds; 2323 seeds were optimized while the remaining 221 were omitted due to their phase $\alpha(T^m)$ exceeding $\pi/4$. Blue circles show $1 - \mathcal{F}^f$ for all solutions, while red circles show $1 - \mathcal{F}^f$ for the monotonically best and optimal solutions [obtained for

durations depending on $\alpha(T^m)$]. We find the upper bound for the quantum speed limit for the full gate to be $T_{\text{QSL}}^f \leq 0.1377$ ms (see Appendix B 2 for the corresponding time-optimal control). This is faster than the $T^f = 0.215$ using the optimal stagewise solution. The suboptimal plateau is now completely absent and we find an increase in the number of optimal solutions by two orders of magnitude.

Figure 9 shows fidelities and independent single-particle densities when propagated along the time-optimal control at T_{QSL}^m [51]. Although there are no explicit distinct stages after optimizing, remnants of the seed's merge-wait-separate sequence (durations marked for reference) is still visible. For example, the time-optimal control as well as the single-particle densities remain essentially symmetric around the $T^f/2$. The bottom row of data in Table I summarizes figures of merit for various states. The situation is quite different from that in Fig. 7, as the Hilbert-space state trajectory is never close to passing through $|\Phi_i^m\rangle$ (or, equivalently, $|e\rangle|g\rangle$ in the independent-particle picture). Nevertheless, the atomic overlap and interaction around $T^f/2$ remain appreciable as the motional excitations allow for synchronized in-phase oscillations. Finally, $|\Phi_i^m\rangle$ is prepared with $\mathcal{F}^f = 0.99$ at the end duration. Interestingly, the seed that optimized to the time-optimal control initially had only $\mathcal{F}^m = 0.93$ at $T^m = 0.0478$ ms. These numerical observations confirm that the restrictions imposed by the merge-wait-separate approach are indeed unnecessarily restrictive.

The plateau in Fig. 6 suggests the existence of optimal merging controls at even lower durations, which could be uncovered by increasing the number of seeds and more elaborate seeding strategies. However, the fact remains that such solutions can practically always be further improved by subsequently optimizing the full gate. It would be more interesting to investigate the full gate with completely independently generated seeds, as the current optimal solutions inherits at least partially the merge-wait-separate stages. Additionally, the single-particle densities seem to have low velocities near the beginning and the end of the transfer. One can imagine rapidly transforming into the single-well configuration: both atoms are then subject to a large initial acceleration towards each other and will evolve without changing their shape appreciably, as they closely resemble coherent states in a harmonic oscillator. As the atoms approach each other, suppose that the atoms could be decelerated to low momenta such that they oscillate out of phase with low amplitudes around the trap center. This would allow rapid entanglement since identical shapes maximize the interaction Eq. (9). If the necessary relative phase is acquired within a little less than a single or a few oscillation periods, each atom will already have correctly

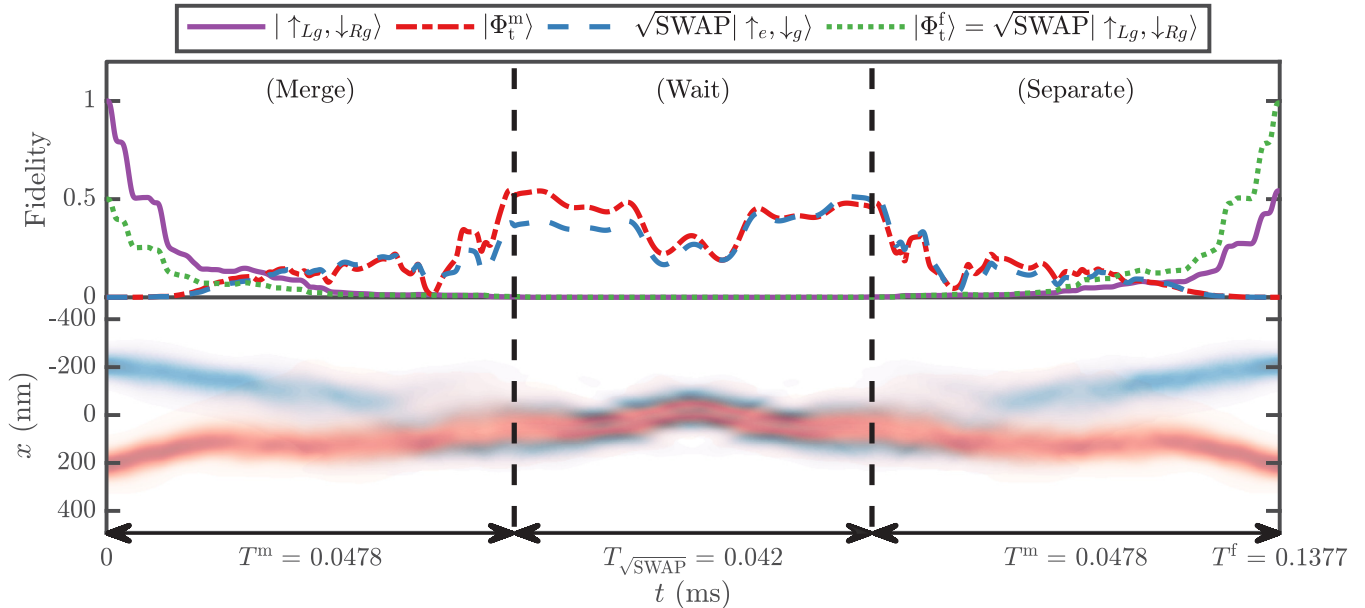


FIG. 9. Full $\sqrt{\text{SWAP}}$ gate operation from the time-optimal full gate control. The initial merge-wait-separate stages for the seed are indicated by the dashed vertical lines. Top: Instantaneous fidelities with various states. Bottom: Corresponding independent single-particle densities [51]. The merging target state $|\Phi_t^m\rangle$ is only partially populated, with at most $\mathcal{F}^m \approx 0.52$. The atoms exhibit in-phase oscillations before the separation onset and enters $|\Phi_t^f\rangle$ with $\mathcal{F}^f = 0.99$ at T^f .

directed opposite momenta at the onset of separation. This is different from the case of in-phase oscillations in Fig. 9, where both atoms must be more delicately exposed to opposite accelerations to correctly separate them. A similar scheme to the above is presented in Refs. [42] and [53] for another type of collisional gate. Whether such strategies are indeed effective in producing better solutions can only be verified by further numerical investigations and is left for future work.

VI. OUTLOOK

There are several areas of possible applications. Closely related to the problem studied in this paper are tweezer geometries for alkalis [23,35] and, more recently, alkaline-earth-like species (AELs) such as ytterbium and strontium [14–16,54]. Briefly, the AELs encode qubits in nuclear spin states while utilizing auxiliary electronic states for state-selective transport and readout in quantum computation architectures [21,26,55]. Pairs of atoms initially reside in individual, radially separated tweezers which are then combined to effect the collisional two-qubit gate. There are several numerical challenges associated with pure tweezer geometries that break the 1D description justified in Appendix A, such as the nonseparability of the potential and the inability to freeze out excitations along the weakly confining axial direction. Neglecting these issues for the moment, one also finds that the local effective coupling $g_{1D} \propto \sqrt{\omega_z(x)}$ becomes imaginary at distances sufficiently far from tweezer centers, calling into question the validity of this model in that regime. One, albeit numerically costly, way to address such difficulties is to explicitly include more spatial degrees of freedom in the simulation. In the case of AELs, the auxiliary electronic degree of freedom introduces both

state-dependent external and interaction potentials [56] and must then also be included explicitly. The latter point may allow much shorter gate durations due to increased flexibility in the external potentials and, e.g., for certain ytterbium isotopes, orders of magnitude larger scattering lengths [26]. A first application for AELs could include a background potential such that a 1D description with spin is a good approximation.

Another application of our analysis may concern qubits, stored either fully [43,44] or partially [46,52] in the motional states of atoms. For the two-qubit gate in these schemes, there is a numerical equivalence to the present problem since the internal degrees of freedom can also be treated implicitly as discussed in Appendix A. These types of problems should therefore be readily addressable with the same methods.

VII. CONCLUSIONS

We have presented and discussed the theory behind collisional $\sqrt{\text{SWAP}}$ gate implementation in cold atoms. Our primary attention is devoted to proper accounting for the relative phase acquired during merging. Optimizing the full gate directly instead of the staged merge-wait-separate sequence is favorable in terms of both final fidelity and optimal trajectories in Hilbert space.

We verified this in an optical lattice geometry. For the merging subproblem, we find $\mathcal{F}^m = 0.99$ at $T_{\text{QSL}}^m = 0.888$ ms, which is an improvement over previous similar results of $\mathcal{F}^m = 0.97$ at $T^m = 0.15$ ms. Nevertheless, a suboptimal plateau of solutions indicates that the merging subproblem is hard to solve and even in the best case the corresponding full gate fidelity is suboptimal at $\mathcal{F}^f = 0.983$ in $T^f = 0.215$ ms. By instead using the merging optimized solutions as seeds for the full gate problem the suboptimal

plateau is eliminated while also yielding a significantly increased number of optimal $\mathcal{F}^f = 0.99$ solutions with durations as low as $T_{\text{QSL}}^f = 0.1377$ ms. The relative phase and the full gate optimization allow separate reductions of the overall gate duration. Both concepts transcend any particular geometry, atomic species, model dimensionality, and type of collisional gate. They may thus be relevant in future work.

ACKNOWLEDGMENTS

This work was funded by the European Research Council, John Templeton Foundation, and the Carlsberg Foundation. The numerical results presented in this work were obtained at the Centre for Scientific Computing, Aarhus.

APPENDIX A: EFFECTIVE 1D DESCRIPTION

Denoting by (\mathbf{r}_i, s_i) the spatial and spin degrees of freedom for the i th particle, the full 3D Hamiltonian describing two interacting spin- $\frac{1}{2}$ particles is

$$\hat{H}_{3\text{D}} = \hat{T} + U(\mathbf{r}_1) + U(\mathbf{r}_2) + U_{\text{int}}(\mathbf{r}_1 - \mathbf{r}_2), \quad (\text{A1})$$

where \hat{T} is the sum of kinetic energy operators over all particle coordinates, $U(\mathbf{r})$ is the single-particle trapping potential, and $U_{\text{int}} = g_{3\text{D}}\delta(\mathbf{r}_1 - \mathbf{r}_2)$ is the interaction potential (we assume isotropic s -wave scattering length $a_s = a_s^{\uparrow\uparrow} = a_s^{\downarrow\downarrow} = a_s^{\uparrow\downarrow}$). Exactly solving the associated equations of motion for $\Phi(\mathbf{r}_1, s_1, \mathbf{r}_2, s_2, t)$ is computationally expensive even for very crude spatial discretizations. For this reason, it is desirable to describe the approximate dynamics in an effective 1D model in which the spin states are treated implicitly. This can be done under the assumption that motion in the remaining spatial axes are frozen out and the Hamiltonian is void of spin terms. In this approximation, the variables separate into the product form

$$\Psi^{(x)}(x_1, x_2, t)\Psi_{\text{gs}}^{(y)}(y_1, y_2)\Psi_{\text{gs}}^{(z)}(z_1, z_2)\chi(s_1, s_2), \quad (\text{A2})$$

$$U(\mathbf{r}) = -V_z \cos^2 kz - V_0 \left[\cos^2 \left(\frac{\beta}{2} \right) \left\{ \cos^2(ky) + \cos^2 \left(kx - \frac{\pi}{2} \right) \right\} + \sin^2 \left(\frac{\beta}{2} \right) \left\{ \cos(ky) + \cos \left(kx - \theta - \frac{\pi}{2} \right) \right\}^2 \right], \quad (\text{A6})$$

$$\omega_z = \sqrt{\frac{2V_z k^2}{m}}, \quad \omega_y(x) = \sqrt{\frac{2V_0 k^2}{m} \left[\cos^2 \left(\frac{\beta}{2} \right) + \sin^2 \left(\frac{\beta}{2} \right) \left\{ 1 + \cos \left(kx - \theta - \frac{\pi}{2} \right) \right\} \right]}. \quad (\text{A7})$$

As ω_z does not depend on x , the z degrees of freedom separate exactly in these approximations. Excitations along this axis can always be suppressed by choosing the independent trap depth V_z to generate sufficiently large vibrational frequencies with associated energy spacings. On the contrary, the separation of the x and y coordinates is only approximate since $\omega_y = \omega_y(x)$. Our calculations of the full 2D single-particle spectrum show that the trapping along x is only slightly weaker than along y , since V_0 is common to both axes. It is therefore much harder to suppress excitations along y than z . Errors induced by the approximate potential separability of x and y is the main limitation of the model, since this

where $\Psi^{(x)}(x_1, x_2, t)$ is the only part of the wave function with a time evolution different from a trivial phase. The motional wave functions in the y and z directions remain in their respective ground state at all times, and the spin wave function remains unchanged. We can then restrict our attention to the nontrivial part of the state $\Phi \sim \Psi^{(x)}$ and drop the superscript as we have done throughout the text. We briefly discuss the steps to obtain (A2) in the following.

The spin degrees of freedom separate exactly since there is no spin dependence in Eq. (A1). The spatial coordinates cannot be separated immediately because U_{int} couples them all. To proceed, we define $V(x) \equiv U(\mathbf{r})|_{\mathbf{r}=\mathbf{x}}$, where $\mathbf{x} \equiv (x, 0, 0)$, and approximate the potential in y and z to be locally harmonic. This allows an approximate 1D description [57] of the interparticle coupling

$$g_{3\text{D}} = \frac{4a_s \pi \hbar}{m} \rightarrow g_{1\text{D}} = 2a_s \hbar \sqrt{\omega_y \omega_z}, \quad (\text{A3})$$

$$\delta(\mathbf{r}_1 - \mathbf{r}_2) \rightarrow \delta(x_1 - x_2). \quad (\text{A4})$$

Importantly, the local harmonic frequency ω_z (ω_y) in the \hat{z} (\hat{y}) direction may become position dependent in x . To calculate these frequencies $U(\mathbf{r})$ is Taylor expanded to second order around point \mathbf{x} . Assuming that \mathbf{x} is a minimum in \hat{y} and \hat{z} one obtains

$$\begin{aligned} U(\mathbf{r}) &\approx U(\mathbf{x}) + \sum_{q=y,z} \left[\frac{1}{2} \partial_{qq} U(\mathbf{r}) \cdot q^2 \right] \Big|_{\mathbf{r}=\mathbf{x}} \\ &= V(x) + \sum_{q=y,z} \frac{1}{2} m \omega_q^2 q^2. \end{aligned} \quad (\text{A5})$$

Comparing the two expressions we obtain the frequencies $\omega_q^2 = \partial_{qq} U(\mathbf{x})/m$. The full 3D potential for the optical lattice [30,48,50] under consideration and corresponding frequencies are

coupling is much larger than the interparticle coupling U_{int} . The quality of the approximation, (A2), can thus be assessed on the independent-particle level. In Fig. 10 we propagate the particle starting in the left ground state over the time-optimal control at T_{QSL}^f and compute the 1D and 2D instantaneous fidelities with the initial state. Their difference corresponds roughly to the leakage out of the ground state in the y direction induced by the nonseparability of the potential. The effects are less pronounced for the particle starting in the right ground state. We have done the same for the optimized control presented in Fig. 8 from Ref. [48] and find similar results.

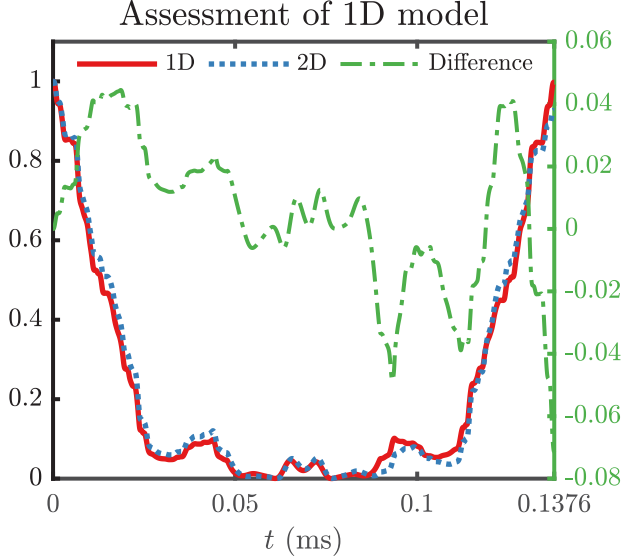


FIG. 10. Comparison of instantaneous fidelities with the initial state in the 1D and 2D case. Their difference roughly corresponds to the leakage out of the ground state in the \hat{y} direction.

APPENDIX B: METHODS

1. Numerics

The simulations and optimization results presented in this paper are produced with the QEngine [58], our recent C++ software package for quantum optimal control.

We simulate rubidium atoms with mass $m_{\text{Rb}} = 87$ amu and assume a state-independent scattering length $a_{\text{Rb}} = 5.45$ nm $\approx 103a_0$ [5,59] where a_0 is the Bohr radius. We restrict our attention to a single unit cell of the lattice defined within $x \in [-1.0, +1.0] \times a$, where $a = 408$ nm $= \lambda/2$ [30] is the lattice site separation for the initial configuration [Fig. 2(a)]. We pad the boundaries slightly such that $x \in [-1.2, +1.2] \times a$ for numerical reasons: in the boundary region a constant $V_{\text{cst}} = \max V(x)$ is used to stabilize the diagonalization. We have verified that the wave function does not enter this nonphysical region when propagated along the optimized controls. The independent lattice in the z direction has strength $V_z = 186$ kHz $\cdot h$ [30]. In the simulation we use the following set of units:

$$\mu_{\text{length}} = a, \quad (\text{B1})$$

$$\mu_{\text{mass}} = m_{\text{Rb}}, \quad (\text{B2})$$

$$\mu_{\text{energy}} = \hbar^2 / (\mu_{\text{mass}} \cdot \mu_{\text{length}}^2), \quad (\text{B3})$$

$$\mu_{\text{time}} = \hbar / \mu_{\text{energy}} = 0.22378 \text{ ms}. \quad (\text{B4})$$

The singlet and triplet states $|\Phi^\pm\rangle \sim |\Psi^\pm\rangle$ are obtained through numerical diagonalization in the discrete $|x_1, x_2\rangle$ representation with uniform grid spacing. The five-diagonal approximation is used for the Laplacian. Propagation is performed using split-step fast Fourier transform, which is fastest if the numbers of spatial grid points are integer powers of 2, e.g., $D \in \{32, 64, 128, 256, 512, 1024\}$. We employ a state absorptive imaginary potential near the grid borders to minimize the effects of the periodic boundary conditions

induced by the split-step fast Fourier transform method. The $\delta(x_1 - x_2)$ in the interaction potential necessitates a very high degree of temporal resolution to reliably produce the correct dynamics [60]. Numerical experiments show that $\delta t = 1.2 \times 10^{-5}$ simulation units is a good value. At this very high temporal resolution the spatial resolution is found to be stable over a surprisingly broad range. Propagating thousands of different controls, the fidelities produced with $D_{\text{max}} = 1024$ and $D = 64$ differ by $(2.2 \pm 2.7) \times 10^{-4}$. Increasing D has almost no effect. However, even at relatively modest D the time discretization still requires $O(10^4)$ steps to reach the durations of interest and optimization is very slow. To significantly speed up the optimization we instead use increasingly finer grids. A grid is defined by the tuple $\{D, \delta t\}$. For the merging subproblem, we optimize on the grids sequentially $\{32, 5 \times 10^{-4}\} \rightarrow \{64, 1 \times 10^{-4}\} \rightarrow \{64, 1.2 \times 10^{-5}\}$. The control is interpolated linearly to the new δt when moving between the grids. This allows performing a large-scale multistarting optimization at a broad range of T on the approximate time scale of several days. Due to memory restrictions we only optimize the full gate on the grids $\{32, 5 \times 10^{-4}\} \rightarrow \{64, 1 \times 10^{-4}\}$ and then simply evaluate on the final grid $\{64, 1.2 \times 10^{-5}\}$ when reporting results.

2. Optimal control

To solve the state transfer problem $|\Phi_0\rangle \rightarrow |\Phi_1\rangle$, we use the L^2 gradient-based GRAPE algorithm with the L-BFGS search direction to minimize the cost functional

$$J[\mathcal{U}] = J_{\mathcal{F}} + J_{\gamma} + J_{\sigma}$$

$$= \frac{1}{2}(1 - \mathcal{F}) + \sum_{i=1}^k \left[\frac{\gamma}{2} \int_0^T \dot{u}_i^2 dt + \frac{\sigma}{2} \int_0^T b(u_i) dt \right]$$

by iteratively improving the set of k control fields (protocols) $\mathcal{U}(t) = \{u_i(t)\}_{i=1}^k$. The gradient is calculated using the adjoint method by introducing an additional Lagrange multiplier term. Minimizing $J_{\mathcal{F}}$ corresponds to maximizing the fidelity $\mathcal{F} = |\langle \Phi_1 | \Phi(T) \rangle|^2 = |\langle \Phi_1 | \hat{U}(\mathcal{U}) | \Phi_0 \rangle|^2$, where \hat{U} is the time evolution operator. J_{γ} adds preference to smoother controls with strength γ and J_{σ} adds preference to controls within specified parameter boundaries $u_i(t) \in [u_{\text{min}}, u_{\text{max}}]_i$ with strength σ . In the latter context, $b(u)$ is a function that is 0 when the boundaries are respected and parabolic when exceeded [58].

As mentioned in the text, a more appropriate measure of the transfer quality for the merging subproblem is the total population $\mathcal{F}' = |\langle \tilde{\Phi}_{e,g}^+ | \Phi(T) \rangle|^2 + |\langle \tilde{\Phi}_{e,g}^- | \Phi(T) \rangle|^2$. This could be directly accommodated in the cost functional by replacing $J_{\mathcal{F}}$ with

$$\frac{1}{2} \left(1 - \mathcal{F}' + \frac{1}{2} \left\{ \frac{|\langle \tilde{\Phi}_{e,g}^+ | \Phi(T) \rangle|^2}{2} - \frac{|\langle \tilde{\Phi}_{e,g}^- | \Phi(T) \rangle|^2}{2} \right\}^2 \right),$$

which is minimized when $|\Phi(T)\rangle$ is fully and equally distributed on the states $|\tilde{\Phi}_{e,g}^\pm\rangle$ independent of the relative phase; see Eq. (24). This replacement requires calculating new Gâteaux derivatives to obtain a new optimality system [58]. Instead of formally doing this we simply use \mathcal{F}' as a stopping condition.

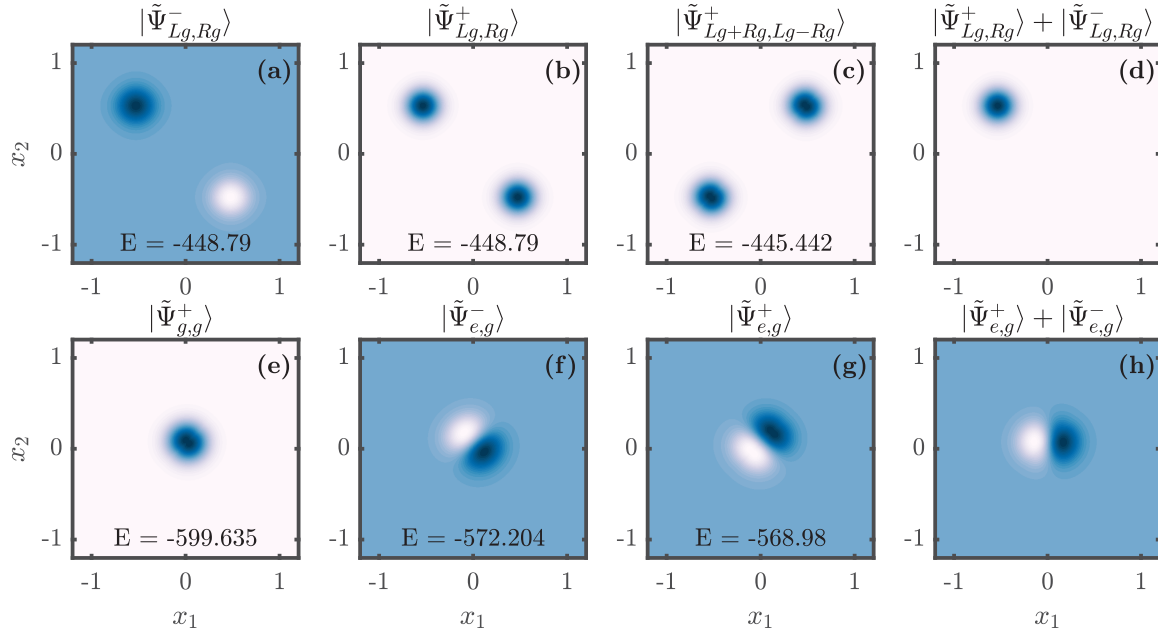


FIG. 11. Numerical two-particle states in the initial configuration (top row) and the merged configuration (bottom row). Lengths are in units of $a = 408$ nm and energies are in units of $\text{kHz} \cdot h$. (a)–(c) Lowest-lying eigenstates. The (ground) states $|\tilde{\Psi}_{Lg,Rg}^{\pm}\rangle$ corresponding to singly occupied wells are degenerate since both wave functions are vanishing for $x_1 = x_2$. The excited state $|\tilde{\Psi}_{Lg+Rg,Lg-Rg}^{\pm}\rangle$ corresponding to doubly occupied wells has an increased energy due to the interaction. (d) Numerical initial state $|\Psi_0\rangle$. (e)–(g) Lowest-lying eigenstates. The symmetric excited state $|\tilde{\Psi}_{e,g}^+\rangle$ has an increased energy compared to the antisymmetric one $|\tilde{\Psi}_{e,g}^-\rangle$. (h) Numerical target state $|\Psi_1^m\rangle$ (here $\alpha_1 = 0$).

The control parameters of the potential Eq. (1) are rescaled as $\mathcal{U} = \{\beta(t), \theta(t), V_0(t)\} \rightarrow \{\beta(t), \theta(t), V_0(t)\} \times \{\beta_{\text{scale}}, \theta_{\text{scale}}, V_{0,\text{scale}}\}$ with values

$$\begin{aligned} \{\beta_{\text{scale}}, \theta_{\text{scale}}, V_{0,\text{scale}}\} &= \{0.52\pi, -0.474\pi, 122 \text{ kHz} \cdot h\}, \\ \mathcal{U}(0) &= \{\beta(0), \theta(0), V_0(0)\} = \{0, 1, 1\}, \\ \mathcal{U}(T) &= \{\beta(T), \theta(T), V_0(T)\} = \{1, 1, 1\}. \end{aligned}$$

The unscaled initial and final control values for the merging subproblem ($\beta = 0 \rightarrow 0.52\pi$, $\theta = -0.474\pi$, $V_0 = 122 \text{ kHz} \cdot h$) are chosen to allow comparison with results in Ref. [48]. Similar values are used in Ref. [49]. Neither paper discusses rescaling. For the full gate problem $\mathcal{U}(T) = \mathcal{U}(0)$.

Figure 11 shows a few select two-particle spatial states. For the separated configuration in Fig. 2(a), $|\tilde{\Psi}_{Lg,Lg}^{\pm}\rangle$ (singly occupied wells) are degenerate, while the interaction increases the energy of $|\tilde{\Psi}_{Lg+Rg,Lg-Rg}^{\pm}\rangle$ (doubly occupied wells) by $\sim 3 \text{ kHz} \cdot h$ as was also reported in Ref. [48].

We include a regularization term with $\gamma = 10^{-7}$ for all controls and a boundary term to constrain $\{-\infty, 0, 0.2\} \leq \{\beta(t), \theta(t), V_0(t)\} \leq \{+\infty, 2.1, 1.15\}$ with $\sigma = 10^5$ such that the adjacent lattice unit cells do not mix and V_0 remains reasonably lower than V_z (see Appendix A). Optimization seeds for merging are generated by perturbing a reference control with $M \sim 40$ – 60 random sine functions of increasing harmonic frequency with random weighting and overall normalization. The reference control was heuristically chosen such that the seed cost is on average decreased. As discussed

in the text, the optimized merging controls are used as seeds for the full gate optimization. In both cases we optimize the seeds until they exceed the figure of merit threshold, converge to a local minimum, or exceed a wall time limit of 7 days. Figures 12 and 13 shows the time-optimal controls for the merging and full gate problems, respectively [51].

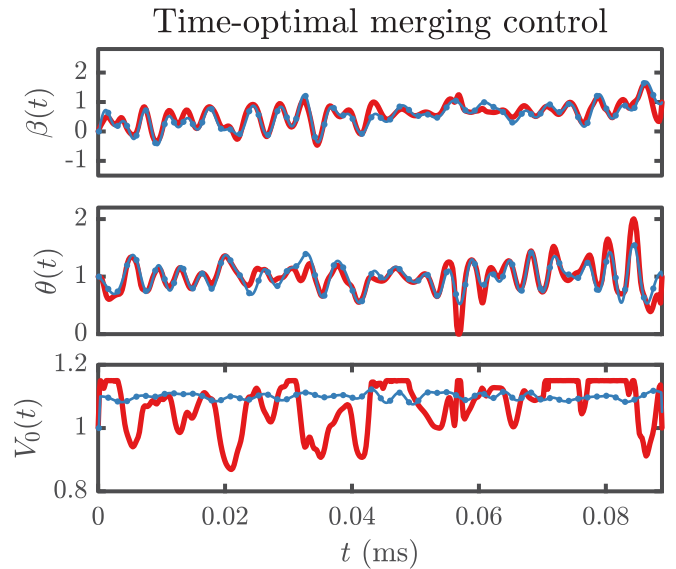


FIG. 12. The set of (scaled) optimal controls and their seed at the quantum speed limit bound $T_{\text{QSL}}^m = 0.0888$ ms. Thin dotted blue line: Initial control. Thick red line: Optimized control.

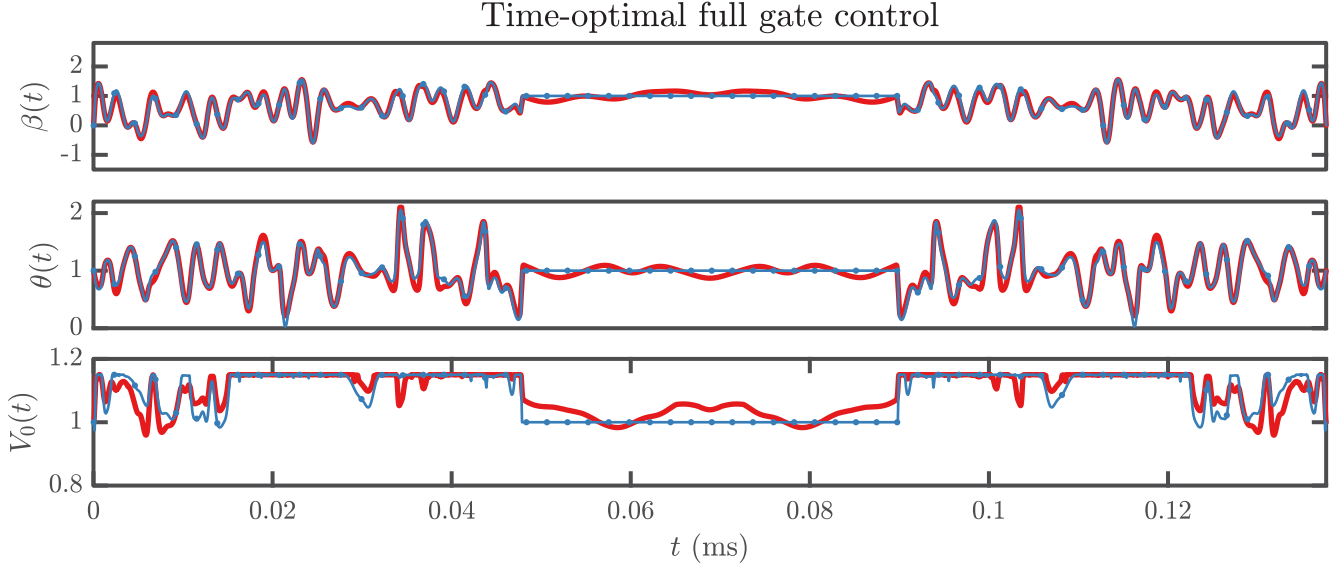


FIG. 13. The set of (scaled) optimal controls and their seed at the quantum speed limit bound $T_{\text{QSL}}^f = 0.1377$ ms. Thin dotted blue line: Initial control. Thick red line: Optimized control.

APPENDIX C: SPIN EXCHANGE HAMILTONIAN

The collisional effect modeled by Eq. (2) is purely spatial, which allowed us to treat the spin states implicitly. However, if the trapping geometry is static and the spatial state is a superposition on the form $|\tilde{\Phi}_{a,b}^+\rangle + |\tilde{\Phi}_{a,b}^-\rangle$ we can describe the dynamics with an effective spin Hamiltonian $\hat{H}_{\text{spin}} = J_{\text{ex}} \cdot \hat{S}_1 \otimes \hat{S}_2$, where \hat{S}_i are spin operators and J_{ex} is the exchange energy. The matrix representation of \hat{H}_{spin} in the standard computational basis $\{|\downarrow, \downarrow\rangle \doteq \mathbf{e}_1, |\uparrow, \downarrow\rangle \doteq \mathbf{e}_2, |\downarrow, \uparrow\rangle \doteq \mathbf{e}_3, |\uparrow, \uparrow\rangle \doteq \mathbf{e}_4\}$ is

$$\hat{H}_{\text{spin}} \doteq \frac{J_{\text{ex}} \hbar^2}{4} \begin{bmatrix} 1 & 0 & 0 & 0 \\ 0 & -1 & 2 & 0 \\ 0 & 2 & -1 & 0 \\ 0 & 0 & 0 & 1 \end{bmatrix}, \quad (\text{C1})$$

where \mathbf{e}_i are standard unit vectors. Clearly the computational basis states are not eigenstates of \hat{H}_{spin} unless $J_{\text{ex}} = 0$. Diagonalization of Eq. (C1) yields energies and corresponding

states

$$E^- = -\frac{3}{4} J_{\text{ex}} \hbar^2 : \quad \chi^- = \frac{1}{\sqrt{2}} (\mathbf{e}_2 - \mathbf{e}_3),$$

$$E^+ = +\frac{1}{4} J_{\text{ex}} \hbar^2 : \mathbf{e}_1, \quad \chi^+ = \frac{1}{\sqrt{2}} (\mathbf{e}_2 + \mathbf{e}_3), \quad \mathbf{e}_4,$$

with three degenerate states corresponding to E^+ . The χ^\pm states are exactly the spin singlet and triplet spin states with an energy difference of $\tilde{U} = J_{\text{ex}}$, while $\chi^{\uparrow\uparrow} = \mathbf{e}_1$ and $\chi^{\downarrow\downarrow} = \mathbf{e}_4$ are the remaining triplet spin states with a nonzero net spin. In this effective spin model, it is the spatial degree of freedom that is treated implicitly. Thus, the time evolution for the initially prepared state $|\uparrow_a, \downarrow_b\rangle = |\tilde{\Phi}_{a,b}^+\rangle + |\tilde{\Phi}_{a,b}^-\rangle$ is

$$\begin{aligned} |\tilde{\Phi}(t)\rangle &= e^{-\frac{i\hat{H}_{\text{spin}}t}{\hbar}} |\uparrow_a, \downarrow_b\rangle = e^{-\frac{i\hat{H}_{\text{spin}}t}{\hbar}} [|\tilde{\Phi}_{a,b}^+\rangle + |\tilde{\Phi}_{a,b}^-\rangle] \\ &= |\tilde{\Psi}_{a,b}^+\rangle e^{-\frac{i\hat{H}_{\text{spin}}t}{\hbar}} |\chi^+\rangle + |\tilde{\Psi}_{a,b}^-\rangle e^{-\frac{i\hat{H}_{\text{spin}}t}{\hbar}} |\chi^-\rangle \\ &= e^{-\frac{iE^+t}{\hbar}} |\tilde{\Psi}_{a,b}^+\rangle |\chi^+\rangle + e^{-\frac{iE^-t}{\hbar}} |\tilde{\Psi}_{a,b}^-\rangle |\chi^-\rangle \\ &\rightarrow |\tilde{\Phi}_{a,b}^+\rangle + e^{i\alpha(t)} |\tilde{\Phi}_{a,b}^-\rangle, \end{aligned}$$

where $\alpha(t) = J_{\text{ex}}t/\hbar$ and we have ignored a global phase. This model exactly reproduces the dynamics from Eq. (19).

-
- [1] S. Chu, *Nature* **416**, 206 (2002).
 [2] I. Bloch, J. Dalibard, and W. Zwerger, *Rev. Mod. Phys.* **80**, 885 (2008).
 [3] J. F. Sherson, C. Weitenberg, M. Endres, M. Cheneau, I. Bloch, and S. Kuhr, *Nature* **467**, 68 (2010).
 [4] C. Weitenberg, M. Endres, J. F. Sherson, M. Cheneau, P. Schauß, T. Fukuhara, I. Bloch, and S. Kuhr, *Nature* **471**, 319 (2011).
 [5] A. Kaufman, B. Lester, C. Reynolds, M. Wall, M. Foss-Feig, K. Hazzard, A. Rey, and C. Regal, *Science* **345**, 306 (2014).
 [6] Y. Wang, X. Zhang, T. A. Corcovilos, A. Kumar, and D. S. Weiss, *Phys. Rev. Lett.* **115**, 043003 (2015).
 [7] H. Kim, W. Lee, H.-g. Lee, H. Jo, Y. Song, and J. Ahn, *Nat. Commun.* **7**, 13317 (2016).
 [8] M. Endres, H. Bernien, A. Keesling, H. Levine, E. R. Anschuetz, A. Krajenbrink, C. Senko, V. Vuletic, M. Greiner, and M. D. Lukin, *Science* **354**, 1024 (2016).
 [9] D. Barredo, S. De Léséleuc, V. Lienhard, T. Lahaye, and A. Browaeys, *Science* **354**, 1021 (2016).
 [10] W. Lee, H. Kim, and J. Ahn, *Opt. Express* **24**, 9816 (2016).

- [11] A. Kumar, T.-Y. Wu, F. Giraldo, and D. S. Weiss, *Nature* **561**, 83 (2018).
- [12] D. Barredo, V. Lienhard, S. de Léséleuc, T. Lahaye, and A. Browaeys, *Nature* **561**, 79 (2018).
- [13] D. Ohl de Mello, D. Schäffner, J. Werkmann, T. Preuschoff, L. Kohfahl, M. Schlosser, and G. Birkl, *Phys. Rev. Lett.* **122**, 203601 (2019).
- [14] S. Saskin, J. T. Wilson, B. Grinkemeyer, and J. D. Thompson, *Phys. Rev. Lett.* **122**, 143002 (2019).
- [15] M. A. Norcia, A. W. Young, and A. M. Kaufman, *Phys. Rev. X* **8**, 041054 (2018).
- [16] A. Cooper, J. P. Covey, I. S. Madjarov, S. G. Porsev, M. S. Safronova, and M. Endres, *Phys. Rev. X* **8**, 041055 (2018).
- [17] G. K. Brennen, C. M. Caves, P. S. Jessen, and I. H. Deutsch, *Phys. Rev. Lett.* **82**, 1060 (1999).
- [18] D. P. DiVincenzo, *Fortschritte Physik Progress of Physics* **48**, 771 (2000).
- [19] D. Jaksch, J. I. Cirac, P. Zoller, S. L. Rolston, R. Côté, and M. D. Lukin, *Phys. Rev. Lett.* **85**, 2208 (2000).
- [20] M. D. Lukin, M. Fleischhauer, R. Cote, L. M. Duan, D. Jaksch, J. I. Cirac, and P. Zoller, *Phys. Rev. Lett.* **87**, 037901 (2001).
- [21] A. J. Daley, M. M. Boyd, J. Ye, and P. Zoller, *Phys. Rev. Lett.* **101**, 170504 (2008).
- [22] A. Negretti, P. Treutlein, and T. Calarco, *Quant. Info. Proc.* **10**, 721 (2011).
- [23] C. Weitenberg, S. Kuhr, K. Mølmer, and J. F. Sherson, *Phys. Rev. A* **84**, 032322 (2011).
- [24] P.-I. Schneider and A. Saenz, *Phys. Rev. A* **85**, 050304(R) (2012).
- [25] N. B. Jørgensen, M. G. Bason, and J. F. Sherson, *Phys. Rev. A* **89**, 032306 (2014).
- [26] G. Pagano, F. Scazza, and M. Foss-Feig, *Adv. Quantum Technol.* **2**, 1800067 (2019).
- [27] T. Xia, M. Lichtman, K. Maller, A. W. Carr, M. J. Piotrowicz, L. Isenhower, and M. Saffman, *Phys. Rev. Lett.* **114**, 100503 (2015).
- [28] Y. Wang, A. Kumar, T.-Y. Wu, and D. S. Weiss, *Science* **352**, 1562 (2016).
- [29] O. Mandel, M. Greiner, A. Widera, T. Rom, T. W. Hänsch, and I. Bloch, *Nature* **425**, 937 (2003).
- [30] M. Anderlini, P. J. Lee, B. L. Brown, J. Sebby-Strabley, W. D. Phillips, and J. Porto, *Nature* **448**, 452 (2007).
- [31] T. Wilk, A. Gaëtan, C. Evellin, J. Wolters, Y. Miroshnychenko, P. Grangier, and A. Browaeys, *Phys. Rev. Lett.* **104**, 010502 (2010).
- [32] X. L. Zhang, L. Isenhower, A. T. Gill, T. G. Walker, and M. Saffman, *Phys. Rev. A* **82**, 030306(R) (2010).
- [33] L. Isenhower, E. Urban, X. L. Zhang, A. T. Gill, T. Henage, T. A. Johnson, T. G. Walker, and M. Saffman, *Phys. Rev. Lett.* **104**, 010503 (2010).
- [34] K. M. Maller, M. T. Lichtman, T. Xia, Y. Sun, M. J. Piotrowicz, A. W. Carr, L. Isenhower, and M. Saffman, *Phys. Rev. A* **92**, 022336 (2015).
- [35] A. Kaufman, B. Lester, M. Foss-Feig, M. Wall, A. Rey, and C. Regal, *Nature* **527**, 208 (2015).
- [36] Y.-Y. Jau, A. Hankin, T. Keating, I. Deutsch, and G. Biedermann, *Nat. Phys.* **12**, 71 (2016).
- [37] H. Levine, A. Keesling, A. Omran, H. Bernien, S. Schwartz, A. S. Zibrov, M. Endres, M. Greiner, V. Vuletić, and M. D. Lukin, *Phys. Rev. Lett.* **121**, 123603 (2018).
- [38] A. Browaeys, D. Barredo, and T. Lahaye, *J. Phys. B: At. Mol. Opt. Phys.* **49**, 152001 (2016).
- [39] M. Saffman, T. G. Walker, and K. Mølmer, *Rev. Mod. Phys.* **82**, 2313 (2010).
- [40] M. Saffman, *J. Phys. B: At. Mol. Opt. Phys.* **49**, 202001 (2016).
- [41] D. Jaksch, H.-J. Briegel, J. I. Cirac, C. W. Gardiner, and P. Zoller, *Phys. Rev. Lett.* **82**, 1975 (1999).
- [42] T. Calarco, E. A. Hinds, D. Jaksch, J. Schmiedmayer, J. I. Cirac, and P. Zoller, *Phys. Rev. A* **61**, 022304 (2000).
- [43] K. Eckert, J. Mompart, X. X. Yi, J. Schliemann, D. Bruß, G. Birkl, and M. Lewenstein, *Phys. Rev. A* **66**, 042317 (2002).
- [44] J. Mompart, K. Eckert, W. Ertmer, G. Birkl, and M. Lewenstein, *Phys. Rev. Lett.* **90**, 147901 (2003).
- [45] M. A. Cirone, A. Negretti, T. Calarco, P. Krüger, and J. Schmiedmayer, *Eur. Phys. J. D - At. Mol. Opt. Plasma Phys.* **35**, 165 (2005).
- [46] E. Charron, M. A. Cirone, A. Negretti, J. Schmiedmayer, and T. Calarco, *Phys. Rev. A* **74**, 012308 (2006).
- [47] D. Hayes, P. S. Julienne, and I. H. Deutsch, *Phys. Rev. Lett.* **98**, 070501 (2007).
- [48] G. De Chiara, T. Calarco, M. Anderlini, S. Montangero, P. J. Lee, B. L. Brown, W. D. Phillips, and J. V. Porto, *Phys. Rev. A* **77**, 052333 (2008).
- [49] M. Mundt and D. J. Tannor, *New J. Phys.* **11**, 105038 (2009).
- [50] M. Anderlini, J. Sebby-Strabley, J. Kruse, J. V. Porto, and W. D. Phillips, *J. Phys. B: At. Mol. Opt. Phys.* **39**, S199 (2006).
- [51] Visit <https://www.quatomic.com/publications/> for animations of the single-particle densities.
- [52] E. Charron, E. Tiesinga, F. Mies, and C. Williams, *Phys. Rev. Lett.* **88**, 077901 (2002).
- [53] P. Treutlein, T. W. Hänsch, J. Reichel, A. Negretti, M. A. Cirone, and T. Calarco, *Phys. Rev. A* **74**, 022312 (2006).
- [54] M. Saffman, *Nature* **567**, 468 (2019).
- [55] A. J. Daley, *Quant. Info. Proc.* **10**, 865 (2011).
- [56] A. V. Gorshkov, M. Hermele, V. Gurarie, C. Xu, P. S. Julienne, J. Ye, P. Zoller, E. Demler, M. D. Lukin, and A. Rey, *Nat. Phys.* **6**, 289 (2010).
- [57] M. Olshanii, *Phys. Rev. Lett.* **81**, 938 (1998).
- [58] J. Sørensen, J. Jensen, T. Heinzl, and J. Sherson, *Comput. Phys. Commun.* **243**, 135 (2019).
- [59] P. S. Julienne, F. H. Mies, E. Tiesinga, and C. J. Williams, *Phys. Rev. Lett.* **78**, 1880 (1997).
- [60] Alternatively one could approximate

$$\delta(x_1 - x_2) \approx \frac{1}{\sqrt{2\pi\epsilon}} e^{-(x_1 - x_2)^2/2\epsilon^2} \quad (C2)$$

for sufficiently small ϵ .